Integrative multi-omics analysis reveals molecular landscape associated with chronic lipid accumulation following contusive spinal cord injury

Xin-Qiang Yao
Nanfang hospital, Southern Medical University
Jia-Ying Chen
Nanfang hospital, Southern Medical University
Zi-Han Yu
Nanfang hospital, Southern Medical University
Zu-Cheng Huang
Nanfang hospital, Southern Medical University
Regan Hamel
University of Cambridge
Jun-Hao Liu
Guangzhou First People's Hospital, School of Medicine, South China University of Technology
Xing Shen
Nanfang hospital, Southern Medical University
Yong-Er Wang
Southern Medical University
Yong-Qiang Zeng
Nanfang hospital, Southern Medical University
Zhi-Ping Huang
Nanfang hospital, Southern Medical University
Yan-Meng Lu
Southern Medical University
Zhi-Tao Zhou
Southern Medical University
Cui-Ting Liu
Southern Medical University
Jun-Min Shi
Southern Medical University
Luca Peruzzotti-Jametti
Department of Clinical Neurosciences, University of Cambridge, UK
Stefano Pluchino

University of Cambridge

Qing-An Zhu

Nanfang hospital, Southern Medical University

Jian-Ting Chen (chenjt@smu.edu.cn)

Nanfang hospital, Southern Medical University

Article

Keywords: Multi-omics, Lipid accumulation, Lipid droplets, Cholesterol metabolism, Remyelination, Spinal cord injury

Posted Date: January 4th, 2023

DOI: https://doi.org/10.21203/rs.3.rs-2437316/v1

Additional Declarations: There is **NO** Competing Interest.

Integrative multi-omics analysis reveals molecular landscape associated with chronic lipid accumulation following contusive spinal cord injury

Xin-Qiang Yao[1†], Jia-Ying Chen[2†], Zi-Han Yu[1,] Zu-Cheng Huang[1], Regan Hamel[3], Jun-Hao Liu[4], Xing Shen[1], Yong-Er Wang[5], Yong-Qiang Zeng[1], Zhi-Ping Huang[1], Yan-Meng Lu[5], Zhi-Tao Zhou[5], Cui-Ting Liu[5], Jun-Min Shi[5], Luca Peruzzotti-Jametti[3], Stefano Pluchino[3], Qing-An Zhu[1], Jian-Ting Chen[1*]

[1]Division of Spine Surgery, Department of Orthopaedics, Nanfang hospital, Southern Medical University, Guangzhou, Guangdong, China

[2]Comprehensive Ward, Nanfang hospital, Southern Medical University, Guangzhou, Guangdong, China

[3]Department of Clinical Neurosciences, University of Cambridge, Cambridge, UK

[4]Division of Spine Surgery, Department of Orthopaedics, Guangzhou First People's Hospital, School of Medicine, South China University of Technology, Guangzhou, Guangdong, China

[5]Central Laboratory, Southern Medical University, Guangzhou, Guangdong, China

*** Correspondence:**

Jian-Ting Chen

chenjt@smu.edu.cn

[†]These authors contributed equally to this study.

Conflict of Interest

The authors declare no competing financial and/or non-financial interests.

Author Contributions

XQ Yao, JY Chen, QA Zhu and JT Chen conceived and designed the work. XQ Yao, ZH Yu, ZC Huang, JH Liu, Xing Shen, YQ Zeng and ZP Huang performed experiments. RH, LPJ and SP helped with review and commentary of the draft. YM Lu and ZT Zhou helped perform the transmission electron microscopy analyses. YE Wang, CT Liu and JM Shi helped perform the lipidomic and proteomic experiments and analyses. XQ Yao, JY Chen, and JT Chen analyzed the data and wrote the manuscript. All authors reviewed and approved the submitted article.

Acknowledgments

JT Chen is supported by National Natural Science Foundation of China (82172492), and the Science and Technology Planning Project of Guangdong Province, China (2017B010110012). XQ Yao is supported by GuangDong Basic and Applied Basic Research Foundation (2022A1515111184). ZC Huang is supported by National Natural Science Foundation of China (81902217). JH Liu is supported by Guangzhou Science and Technology Plan Project (202102021244). The authors thank Dr. Jianming Zeng (University of Macau), and all the members of his bioinformatics team, biotrainee, for generously sharing their experience and codes.

Abstract

Lipid metabolism is a critical process that occurs in the lipid-rich spinal cord during damage and repair. Here, we integrated ultrastructural characteristics with multi-omics analysis as well as transcriptomic, untargeted, targeted proteomic, lipidomic, and N6-methyladenosine (m^6A) epitranscriptomic profiling in a clinically relevant spinal cord injury (SCI) model. We observed lipid accumulation, lysosome-based autophagy of lipid droplets, and remyelination in the lesion of the chronic phase. The analysis also revealed molecular alterations associated with the enhancement of glycolysis, tricarboxylic acid cycle, and fatty acid metabolism, marked increases in triglyceride species with C16:0 fatty acyl chains, and adaptive changes in cholesterol metabolism. These changes included decreased uptake of cholesterol through *Mylip* upregulation, decreased synthesis through downregulation of *Fdps* and *Hmgcs1*, and increased efflux through *Apoe* upregulation. Among these, *Mylip* and *Hmgcs1* are regulated by m^6A methylation. Altogether, our findings revealed endogenous mechanisms in response to microenvironment changes, highlighting the potential of exploring lipid regulators for SCI treatment.

Key Words: Multi-omics, Lipid accumulation, Lipid droplets, Cholesterol metabolism, Remyelination，Spinal cord injury.

Introduction

In most cases, patients with spinal cord injury (SCI) have poor neurological outcomes and require specialized care, which imposes an enormous burden on individuals, families, and society[1]. Due to the lack of effective drugs, current treatment strategies include timely surgery, rehabilitation, and supportive treatment[2]. Recent multinational clinical trials, conducted over the last two decades, have reported no progress in neurological recovery following SCI[3]. The primary trauma induces a cascade of secondary damages, including ischemia, oxidative stress, neuroinflammation, and glutamate neurotoxicity[4]. Three different phases occur following SCI[5], and the lesions can be divided into three different regions: lesion core, surrounding lesion rim, and spared intact areas[6]. In the chronic phase, the lesion core comprises the extracellular matrix (ECM) and fibrotic scar generated by multiple nonneural cells[7]. The lesion rim is characterized by "astrocyte scars," pro-inflammatory microglia, and neuronal oxidative injury[6]. Spontaneous remyelination through newly formed oligodendrocytes and Schwann cells is crucial for the restoration of metabolic support and energy-efficient conduction following myelin loss[8]. Therefore, the stalled progress and complex pathophysiological changes urgently warrant a comprehensive understanding of the pathological events and the underlying molecular alterations following SCI.

Integrative multi-omics analysis involving lipidomics, transcriptomics, and proteomics is emerging as a promising approach for understanding brain pathology[9]. Furthermore, a recent study showed an important role for N6-methyladenosine (m^6A) methylation in neurodegenerative diseases[10]. Myelin contains a high lipid composition, including fatty acids, glycosphingolipids, and cholesterol[11]. Our previous proteomic profiling in a rat SCI model demonstrated that lipid regulation pathways were main functions of upregulated proteins in the early phase[12]. Moreover, we identified apolipoprotein E (*Apoe*) as a hub gene of phagocytes using a single-cell RNA sequencing dataset and observed increased lipid droplets (LDs) and cholesterol crystals in $Apoe^{-/-}$ mice following SCI[13]. Lipid metabolism plays an important role in SCI, yet the underlying molecular links and regulatory mechanisms remain unclear.

In the present study, we used a series of transmission electron microscopy (TEM) images to analyze the ultrastructural characteristics of a spinal cord hemi-contusion injury mouse model with high precision and stability. We then identified specific protein modules in the chronic phase using weighted gene co-expression network analysis (WGCNA) and temporal clustering analysis in the untargeted proteomic analysis of 24 samples collected at different time points. Furthermore, we performed an integrated analysis of lipidomics, transcriptomics, targeted proteomics, and m^6A epitranscriptomics to develop the molecular landscape of the chronic phase of SCI (Figure 1B).

Results

Dynamic microenvironment in ultrastructural changes

The microenvironment dynamically changes after SCI. To investigate the pathological events from an ultrastructural perspective, a time-course analysis of the TEM images was conducted in a mouse SCI model (Figure 1A). Three days after SCI, the breakdown of the blood-spinal cord barrier led to hemorrhage and infiltration of leukocytes (Figure 1C). The red blood cells were engulfed by activated microglia (Figure 1E). Monocyte-derived macrophages showed relatively large nuclei, small bodies, and well-developed organelles (Figure 1D). We observed that the lesion epicenter contained spaced homogeneous fluids, which might be the lipid released in situ after myelin injury (Figure 1F). Seven days following SCI, macrophages became lipid-laden foam cells because of their powerful phagocytic capacity (Figure 1G-H). The endoplasmic reticulum was well-developed, which controlled the biosynthesis of LDs (Figure 1J). Vascular endothelial cells also phagocytized myelin debris with increased the numbers of LDs and lysosomes (Figure 1I). Six weeks after SCI, cystic cavities were partially replaced by fibrotic scar tissue and LDs (Figure 1K), along with spontaneous remyelination by oligodendrocytes and Schwann cells (Figure 1L, N), and newly formed microvessels (Figure 1M). Notably, we observed that substantial amounts of lipids were not degraded within the lesion core. Similar to the pathological events at 6 weeks post injury (wpi), fibrotic scars, newly formed myelin sheaths, and LDs were observed in the injury core at 16-wpi (Figure 1O, P, and R). Typical pericytes and fibroblasts were observed in the injury core, which formed a fibrotic scar after SCI (Figure 1Q)[30]. Consistent with previous literature, three days post injury (dpi) was regarded as the acute phase time point, 7-dpi was regarded as the subacute phase time point, and 6-wpi was regarded as the chronic phase time point in the present study[5].

Unsupervised clustering analysis identified protein modules associated with chronic phase of SCI

To investigate the molecular signatures during wound repair and regeneration, we performed an untargeted proteomic profiling of spinal cord tissues collected from 3-dpi, 7-dpi and 6-wpi. We identified 3700 proteins, and 1755 proteins were subjected to subsequent analysis after data quality control. We used WGCNA to distinguish these proteins into eight distinct modules representing networks of highly interconnected proteins (Figure 2A). Notably, the blue module was highly correlated with the 6-wpi samples (305 proteins, $r = 0.96$, $P = 2\times10^{-13}$), suggesting that the proteins and pathways in the blue module were significantly associated with the sample traits of chronic SCI (Figure 2B). Kyoto Encyclopedia of Genes and Genomes (KEGG) pathway analysis showed that the blue module was significantly enriched in multiple neurodegenerative diseases, oxidative phosphorylation, the HIF-1 signaling pathway, and other metabolic pathways, including carbon metabolism, glycolysis/gluconeogenesis, pyruvate metabolism, fatty acid degradation, and the citrate

cycle (Figure 2C). The chord diagram showed that phosphofructokinase enzyme (*Pfkl* and *Pfkm*), the key enzyme in the first committing step of glycolysis, was significantly upregulated at 6-wpi (Figure 2D). Isocitrate dehydrogenase-2 (*Idh2*), a mitochondrial enzyme that converts isocitrate to α-ketoglutarate (α-KG) in the tricarboxylic acid (TCA) cycle, was also significantly upregulated at 6-wpi. Glycolysis and the TCA cycle can provide fuel for the biosynthesis of fatty acids. Thus, the protein module highly correlated with chronic SCI indicated metabolic reprogramming in spinal cord tissues.

To study the dynamic protein expression patterns at different phases, we applied the fuzzy c-means algorithm and found six stable and distinct clusters (Figure 2E). Cluster 4 contained 300 proteins, with upregulated expression at 3-dpi, peaked at 7-dpi, and remained high at 6-wpi. Interestingly, KEGG pathway enrichment analysis revealed activation of lysosomes, phagosomes along with fatty acid metabolism, ferroptosis, autophagy, pyruvate metabolism, and biosynthesis of unsaturated fatty acids (Figure 2F). Acetyl-CoA carboxylase alpha (*Acaca*) catalyzes carboxylation of acetyl-CoA, which is a rate-limiting step in the biosynthesis of fatty acids. *Acaca* was significantly upregulated at 3-dpi, 7-dpi and 6-wpi. The composition of lysosomes, such as *Lamp1*, *Lamp2*, and hydrolases (*Ctsb*, *Ctsd*, *Ctsz*, and *Hexb*), was significantly upregulated after SCI. Furthermore, cluster 6 (319 proteins), with a gradually increasing expression trend, was significantly enriched in glycolysis/gluconeogenesis (e.g., *Pfkl* and *Pfkm*), PPAR signaling pathway (e.g., *Sorbs1*, *Cpt2*, *Cpt1a*, *Fabp7*, and *Dbi*), fatty acid metabolism (e.g., *Cpt2* and *Cpt1a*), pyruvate metabolism (e.g., *Aldh3a2* and *Me2*), and AMPK signaling pathway (e.g., *Pfkl*, *Cpt1a*, and *Pfkm*; Figure 2G). *Cpt1a* and *Cpt2* are PPARα-regulated key enzymes of fatty acid oxidation (FAO). Together with the pathological manifestations of lipid accumulation, changes in metabolism-related proteins in the SCI microenvironment, especially in the chronic phase, may lead to altered lipid metabolites.

Triglyceride (TG) increased significantly in the chronic phase of SCI

To investigate the underlying lipidomic profile in the chronic phase of SCI, we performed untargeted lipidomic analysis of the spinal cord tissues collected at 6-wpi. Overall, 1038 individual lipid species were identified (Figure 3B). Half of the lipid species were glycerophospholipids (GP), especially phosphatidylcholine (PC) and phosphatidylethanolamine (PE), which is consistent with the brain lipid composition[9]. Principal component analysis (PCA) showed that the lipidomic profile at 6-wpi was distinct from that in the sham group (Figure 3C). The top 20 critical lipids included PG (18:1/20:4), LPE (22:0), LPE (24:1), LPE (22:2), LPS (20:1), PI (17:1/20:4), LPC (21:0), PG (20:4/20:4), LPC (23:0), TG (16:0/17:0/20:4), TG (15:0/16:0/22:6), LPS (18:1), PC (20:1/22:6), PS (17:0/20:4), LPS (20:0), LPC (17:0), MGDG (18:1/18:1), LPE (19:1), CL (23:0/18:1/20:4/22:6), and PG (20:1/18:1) (Figure 3D). Half of these lipid species were lysoglycerophospholipids (LysoGP), which were significantly upregulated at 6-wpi. LysoGP is produced by

147 $cPLA_2$, which is activated and treated as a therapeutic target for SCI[31]. Among the 29 classes of spinal cord
148 lipids, lysophosphatidylethanolamine (LPE), phosphatidylglycerol (PG), lysophosphatidylcholine (LPC),
149 sphingosine (So), monoglyceride (MG), lysophosphatidylserine (LPS), and TG were determined to be
150 significantly altered following SCI (Figure 3E). Notably, TG (16:0/17:0/20:4), TG (20:0p/16:0/21:0), TG
151 (15:0/16:0/22:6), TG (16:0e/18:1/23:0), DG (18:1/23:0), LPE (24:1), TG (16:0e/14:0/16:0), TG
152 (16:0/17:0/22:6) and PG (20:3/22:6) were the top 10 significantly increased lipid species (Figure 3A, F). All
153 TG species had palmitate (C16:0 fatty acyl chains), indicating de novo lipogenesis (DNL) following SCI.
154 Consistent with molecular changes at the protein level, lipidomic analysis showed increased lipogenesis and
155 TG accumulation in the chronic phase of SCI.

156 **Integrated analysis reveals lysosome-based autophagy and cholesterol metabolic process**

157 To further study the molecular mechanisms and functions related to the chronic phase of SCI, we
158 analyzed the transcriptomic and proteomic profiles of the spinal cord samples at 6-wpi. PCA at the RNA and
159 protein levels showed that the 6-wpi and sham samples were well separated (Figure 4A-B). In a total of 1625
160 mRNA-protein pairs, the correlation between RNA and protein was 0.3, indicating a discrepancy between
161 mRNA levels and protein abundance (Figure 4C). At both the RNA and protein levels, we found 47 mutually
162 upregulated genes, five mutually downregulated genes, and only three genes with discordant regulation
163 (Figure 4D). For the mutually upregulated and downregulated genes (Figure 4E), KEGG pathway enrichment
164 analysis showed that these genes were enriched in autophagy (*Lamp2, Ctsd, and Ctsb*), lysosome (*Lamp2,*
165 *Hexb, Ctsz, Ctsd, and Ctsb*), ECM-receptor interaction (*Col1a1, Col1a2, Col6a1, Col6a2*, and *Col6a3*),
166 terpenoid backbone biosynthesis (*Fdps and Hmgcs1*), and the PPAR signaling pathway (*Hmgcs1* and *Sorbs1*;
167 Figure 4F). Interestingly, we did not observe canonical autophagosomes in the TEM images of the 6-wpi
168 samples. Instead, we observed numerous instances of the increased lysosomes wrapping the LDs. As
169 organelles of TG and cholesteryl ester (CE) storage, LDs can be formed in virtually all brain cells[32], and LDs
170 degradation is regulated through autophagy[33]. Compared to the sham group, immunofluorescence staining
171 showed significantly upregulated LC3+ expression colocalized with BODIPY-labeled LDs in F4/80+
172 microglia/macrophages at 6-wpi (Figure 4G-I). TEM images showed that normal microglia were characterized
173 by small size, thin cytoplasm, and rounded and blunt nuclei with heterochromatin (Figure 4J-K). We observed
174 that microglia at 6-wpi contained abundant inclusions, including myelin, LDs, and different stages of
175 lysosomes (Figure 4L). LDs were directly engulfed by the "wrapping lysosomes" without the formation of
176 double-membrane autophagosomes, similar to lipophagy in macrophage-derived foam cells and hepatocytes[34,
177 35]. Therefore, the proteins and lipids of LDs in microglia may be transferred to lysosomes by direct interactions,
178 as in hepatocytes[35].

Hmgcs1 and *Fdps*, two cholesterol synthesis genes that were downregulated in spinal cord astrocytes in the multiple sclerosis model[36], were both decreased at the RNA and protein levels in the present study (Figure 4E). *Apoe*, the carrier of cholesterol efflux, was significantly upregulated, consistent with our previous proteomic analysis in a rat SCI model[12]. These findings indicate an adaptive response in cholesterol metabolism following SCI.

Parallel reaction monitoring (PRM) targeted proteomics

The DEPs at 6-wpi were mainly involved in ECM-receptor interaction, lysosomes, terpenoid backbone biosynthesis, and fatty acid metabolism (Figure 5A). We then applied PRM-targeted proteomics to further verify DEPs related to key functions in the chronic phase of SCI. During data processing, Skyline automatically implemented transition identification of the peptide and peak area integration (Figure 5B-C). The fragment ions with the highest intensities were used for quantification[23]. Several proteins were reliably detected, with a consistent expression trend in both untargeted and targeted proteomics (Figure 5D-K). *Apoe* is upregulated as a hub gene in macrophages and microglia after SCI[13]. *Apod* is a neuroprotective lipid-binding protein with an enhancing antioxidant that prevents lysosomes from membrane permeabilization[37]. *Hexb* is a lysosomal enzyme required for the degradation of ganglioside GM2, and *Hexb* is upregulated in microglia in a vast number of models of neurodegeneration and demyelination[38]. *Lamp1* is a marker of various endocytic organelles[39]. Type I collagen (*Col1a1* and *Col1a2*) is a key factor for scar formation via interaction with the integrin–N–cadherin pathway, and blockade of this interaction reduces scar formation and promotes axonal regrowth after SCI[40]. These results indicate the reliability of label-free proteomic analysis.

m^{6}A modification regulated wound repair and lipid metabolism

To verify the lipid accumulation observed in TEM images, we performed oil red O staining, which specifically labels neutral lipids. Consistently, we found characteristic lipid accumulation in the lesion core and the surrounding rim. The extent and concentration of lipid accumulation peaked at 6-wpi (Figure 6A). m^{6}A modifications reportedly play a crucial role in neurodegenerative diseases and hepatic lipid metabolism[10, 41]. However, whether m^{6}A modifications influence wound repair and lipid metabolism in the spinal cord following injury remains unclear. We used methylated RNA immunoprecipitation and sequencing (MeRIP-seq) to further investigate the m^{6}A profile of spinal cord samples collected at 6-wpi. m^{6}A peaks were characterized by the canonical GGACU motif (Figure 6B) and were mainly distributed near the coding sequence (CDS) and the 3′ untranslated region (3'UTR; Figure 6C). A total of 815 genes with differential m^{6}A peaks were identified at 6-wpi compared to sham samples. Gene Ontology (GO) analysis showed that these genes were mainly involved in biological processes that would be an adaptive response in the chronic phase of SCI, including axonogenesis, response to transforming growth factor beta, fat cell differentiation, regulation

of canonical Wnt signaling pathway (e.g., *Daam2*, a regulator of remyelination[42], Figure 6J), autophagy, regulation of lipid metabolic processes, and myelination (Figure 6D). Similarly, KEGG pathway analysis highlighted the involvement of axon guidance, lipid and atherosclerosis, and the TGF-β signaling pathway (e.g., *Tgif1*, Figure 6L) (Figure 6E).

To study the influence on gene expression, we correlated differentially methylated genes with the mRNA and protein levels. The differentially methylated genes overlapped with 6 DEPs and 30 DEGs (Figure 6F). Methylation and gene expression were positively correlated (Figure 6G). Interestingly, we found hypomethylation at multiple m^{6}A sites in the cholesterol synthesis gene *Hmgcs1*, which correlated with a downregulation in mRNA and protein levels after SCI (Figure 6H). Moreover, we observed that *Mylip* (also known as inducible degrader of LDLR, *Idol*) was upregulated by elevated m^{6}A levels (Figure 6I), which might regulate cholesterol homeostasis by reducing LDL cholesterol uptake. Recent research has reported that m^{6}A increases glycolysis in cancer cells via *Pdk4*[43], whose m^{6}A level and expression were also upregulated in the present study (Figure 6G, O). Notably, Maf bZIP transcription factor B (*Mafb*), a key transcription factor for homeostatic microglia[44], exhibited significantly elevated m^{6}A methylation (Figure 6N). Similarly, collagen domain-binding receptor *Lair1* and its ligand *Colec12*, which regulate the homeostasis of monocytes and macrophages[45], showed significant m^{6}A peaks in the 3'UTR (Figure 6M, K). Collectively, these results show that m^{6}A modifications play a crucial role in wound repair and lipid metabolism in the chronic phase of SCI.

Discussion

In this study, we integrated ultrastructural features with multi-omics analysis and revealed m^{6}A methylation regulation of metabolic reprogramming in the chronic phase of SCI. Specifically, our results show that lipid accumulation and remyelination are unique characteristics of the damage and repair process, concomitant with the enhancement of glycolysis, TCA cycle, and fatty acid metabolism. Furthermore, we recognize an adaptive response in cholesterol metabolism, including decreased uptake by the upregulation of *Mylip*, decreased synthesis by the downregulation of *Fdps* and *Hmgcs1*, and increased efflux by the upregulation of *Apoe*, among which, *Mylip* and *Hmgcs1* are regulated by m^{6}A modification (Figure 7).

Recent studies have demonstrated that neuronal and glial damage resolves into fluid-filled cavities in the lesion epicenter of patients with SCI over time[2, 4]. Cysts have either uniform or complex morphologies on MRI images[2]. The mouse model induced by contusion has been useful for simulating pathophysiological changes in traumatic human SCI[4]. Interestingly, we observed through electron microscopy, that there were spaced homogeneous fluids in the lesion core at 3-dpi, and gradually replaced by fibrotic scar, newly formed myelin sheath, and LDs at 6-wpi and 16-wpi. The spinal cord is rich in lipids, and myelin is not the only source

that induces lipid accumulation after contusive SCI[46]. The lipids released following injury must be further degraded and reused. Furthermore, TG accumulation and upregulated proteins related to glycolysis, TCA cycle, and fatty acid biosynthesis indicated DNL in the chronic phase of SCI. Therefore, a lipid-rich microenvironment may promote LD biogenesis to mitigate lipotoxic damage. LDs can store excess lipids and generate free fatty acids via the autophagy-lysosome pathway and hydrolytic enzymes. Free fatty acids can provide energy through FAO or supply essential lipids for remyelination[47]. A recent study demonstrated that blockade of LD biogenesis in microglia led to exacerbated inflammation and defective remyelination in a toxin-based model of demyelination[48]. Research has shifted from TG accumulation to LDs in non-alcoholic fatty liver disease (NAFLD)[49]. Nevertheless, little is known about the role and mechanism of LDs during the repair process of SCI; future intervention studies and multi-omics analyses focusing on LDs are essential.

Myelin contains high levels of cholesterol[11]. Cholesterol homeostasis is regulated by four pathways: biosynthesis, uptake, efflux, and storage[50]. Cholesterol in the central nervous system (CNS) is produced in situ by astrocytes and oligodendrocytes, which are almost separated from the circulation due to the blood–brain barrier[51]. Cellular uptake of cholesterol is mainly mediated by LDLR, and *Mylip* can induce its degradation[50, 52]. Our results indicated that m^{6}A modification is involved in the regulation of cholesterol homeostasis by decreasing cholesterol synthesis and uptake during the chronic phase of SCI. Furthermore, cell types in the CNS are unable to catabolize cholesterol, which must be transported out of the cell or stored in LDs[50, 53]. We observed upregulated *Apoe* expression and LDs accumulation, indicating excessive cholesterol in the epicenter of the lesion. In our recent study, *Apoe* knockout mice showed worse neurological recovery, with more LDs and cholesterol crystals in macrophages and microglia following SCI[13]. Cholesterol bioavailability is essential for remyelination[54]. We observed that remyelination through Schwann cells occurred in the lipid-rich microenvironment. Facilitating cholesterol efflux from phagocytes reportedly improved remyelination by oligodendrocytes in a cuprizone-treated demyelinating model. More recently, promoting cholesterol efflux increased myelination and improved cognition in *Apoe*4/4 targeted-replacement mice, providing a new perspective for treating Alzheimer's disease[54]. Here, we observed that endogenous mechanisms regulating cholesterol metabolism, particularly cholesterol efflux and recycling, might increase remyelination after SCI.

This study has several limitations. For example, we performed a multi-omics analysis of spinal cord tissues, including the epicenter and adjacent areas. Nonetheless, distinct morphology and remarkable cellular complexity in different lesion regions were observed from TEM images; further spatially resolved analysis is required to understand the cellular communities and molecular interactions. In addition, we did not investigate lipidomic and m^{6}A profiles at different phases of SCI. We focused primarily on lipid accumulation during the

chronic phase. Dynamic molecular and epigenetic changes in lipids require further study. Finally, a few cholesterol species were identified, and they were filtered after quality control. Although isopropanol precipitation has proven an excellent sample preparation procedure for untargeted lipidomic profiling[19], the non-polar cholesterol in the spinal cord homogenate might require a specific extraction method. TG accumulation was consistent with the upregulation of fatty acid biosynthesis. Because cholesterol synthesis is downregulated, local cholesterol recycling could be an entry point for future investigations.

Together, our results show lipid accumulation in the lesion of a clinically relevant SCI model, with molecular alterations associated with metabolic reprogramming and epigenetic regulation, pointing to a primary role of lipid metabolism during secondary damage and repair of SCI. Future studies will demonstrate the effects of reducing DNL, stimulating lysosome-based autophagy of LDs, and promoting local cholesterol recycling, thus offering new therapeutic strategies for SCI.

Materials and methods

Mice

All animal experiments were approved by the Laboratory Animal Care and Use Committee of Nanfang Hospital, Southern Medical University, and were performed according to the National Guidelines for the Care and Use of Animals. Male C57BL/6 mice (8 weeks old) were purchased from the Laboratory Animal Center of Southern Medical University and housed in a temperature-controlled environment under a 12-h light-dark cycle with ad libitum access to food and water at the Laboratory Animal Center of Nanfang Hospital.

C5 spinal cord hemi-contusion injury

Mice were anesthetized using isoflurane (3% for induction and 1.5%–2% for maintenance). The surgical procedures were conducted as previously described[14]. Briefly, following the removal of the C5 lamina, mice received contusion SCI using an electromagnetic servo material testing machine (Instron E1000, Instron, United States). The diameter of impact tip was 1.0 mm, and the applied displacement and speed were set to 1.2 mm and 300 mm/s, respectively. In sham-operated control mice, the same surgical procedure was performed without induction of spinal cord contusion.

Transmission electron microscopy

At 3-dpi, 7-dpi, 6-wpi and 16-wpi, mice were deeply anesthetized with sodium pentobarbital and perfused with phosphate-buffered saline (PBS) and 4% paraformaldehyde. Spinal cords were fixed in 2% glutaraldehyde in 0.1 M PBS buffer for 24 h at 4°C. After tissue trimming and rinsing in PBS, post-fixation in osmium tetroxide for 1 h was followed by graded dehydration in ethanol (30%, 50%, 70%, 90%, and 100%),

permeabilization in acetone-Epon mixtures (1:1 for 1 h, 1:2 for 2 h, 1:2 for 3 h, and pure Epon overnight), and embedding in Epon. Samples were sliced into semi-thin (0.2 μm) and ultrathin sections (50–70 nm) using a Leica UC7 ultramicrotome. Semi-thin sections were stained with toluidine blue and imaged using a Leica DM4000 microscope. The ultrathin sections were stained with uranyl acetate and lead citrate. TEM images were acquired using a transmission electron microscope (HITACHI H-7500) equipped with an EMSIS Morada G3 CCD camera.

Label-free proteomic analysis

At 3-dpi, 7-dpi and 6-wpi, the mice were anesthetized and perfused with PBS alone to harvest spinal cord tissues (5 mm rostral to 5 mm caudal to the epicenter). Proteins were extracted from the tissue samples (each group, n=6) using 8 M urea (U4883, Sigma-Aldrich). The concentration of each sample was determined using the bicinchoninic acid assay. Proteins were reduced to a final concentration of 5 mM dithiothreitol (A39255, Thermo Fisher Scientific) at 56°C for 30 min, followed by alkylation with 10 mM iodoacetamide (A39271, Thermo Fisher Scientific) at room temperature (RT) for 30 min in the dark. Proteins were digested in trypsin (V5280, Promega) with a 10 KD FASP filter (VN01H02, Sartorious) at an enzyme-to-protein ratio of 1:50 overnight at 37°C. Data-dependent acquisition (DDA) was performed using an Orbitrap Fusion™ Tribrid™ High-Resolution Mass Spectrometer equipped with an Easy-nLC ™ liquid chromatography system (Thermo Fisher Scientific). Mobile phase A was 0.1% formic acid (FA) and mobile phase B was acetonitrile (ACN):0.1% FA = 4:1. Peptides were separated using a 15 cm×75 μm NanoViper™ C18 column (particle size 2 μm, Thermo Fisher Scientific) at a flow rate of 300 nL/min with a 120 min gradient: (1) 5–10% solvent B for the first 28 min; (2) 10–22% in 55 min; (3) 22– 30% in 27 min; and (4) 100% solvent in the last 10 min. The precursors and fragments were analyzed using an Orbitrap detector operated in positive ion mode with a scan range of 350–1500 m/z.

Raw MS data were analyzed using a Linux-compatible MaxQuant version[15]. The R package "DEP" was applied for data filtration, normalization, imputation and differential protein expression analysis[16]. Differentially expressed proteins (DEPs) were defined by cut-off values ($P < 0.05$, absolute value of fold change >1.5). Clusters of highly correlated proteins across 24 proteomic samples were identified using WGCNA[17]. Protein modules with consistent expression patterns following SCI were identified by fuzzy c-mean clustering using "Mfuzz" package[18].

Untargeted lipidomics

Lipids were extracted from spinal cord tissues (sham group, n=6; 6-wpi group, n=6) using isopropanol precipitation, an excellent sample preparation procedure for high-throughput untargeted lipid profiling using ultra performance liquid chromatography−mass spectrometry (UPLC−MS)[19]. Briefly, tissue homogenate (50

μL each) was precipitated by addition of three volumes of isopropanol precooled to −20°C, followed by vortex mixed for 1 min, incubation at RT for 10 min, storage overnight at −80°C, and centrifuged at 16 000g for 20 min the following day. The quality control sample was constituted by pooling 20 μL of supernatant from each sample. The samples were analyzed using an Orbitrap Fusion™ Tribrid™ High-Resolution Mass Spectrometer (Thermo Fisher Scientific) equipped with a Vanquish™ Flex ultra-high-performance liquid chromatograph (Thermo Fisher Scientific). The extracts were separated using a 150 mm×2.1 mm Acclaim™ C30 chromatographic column (particle size 3 μm, Thermo Fisher Scientific) at a flow rate of 0.3 mL/min at 40°C. Mobile phase A was as follows: 10 mM $HCOONH_4$, 0.1% FA, and ACN: H_2O = 60:40, and mobile phase B comprised 10 mM $HCOONH_4$, 0.1% FA, and isopropanol: ACN = 90:10. The samples were detected in both the positive and negative ion modes. A full scan was obtained at a resolution of 60,000 and m/z values ranging from 200–2000, followed by an MS/MS scan with DDA (dd-MS2, Top Speed) at a resolution of 15,000 in HCD mode.

The lipid species were identified using the Lipid Search 4.1 software (Thermo Fisher Scientific). The expression levels of individual samples were normalized to the protein concentration. Lipidomic analysis was performed using the online MetaboAnalyst tool (www.metaboanalyst.ca)[20]. Principal component analysis (PCA) and orthogonal projections to latent structures discriminant analysis (OPLS-DA) were used to separate the sample groups and identify the characteristic lipids of SCI. The contribution of lipid classes to the OPLS-DA model was evaluated using the variable importance in projection (VIP) score. The most critical lipids were defined using cut-off values ($P < 0.05$, VIP >1). The Student's t-test was used to compare the 6-wpi group with the sham group.

Transcriptomic analysis

Total RNA was extracted from spinal cord tissues (sham group, n=5; 6-wpi group, n=5). mRNA was purified using poly T oligo-attached magnetic beads. The library fragments were purified with the AMPure XP system (Beckman Coulter, USA), followed by PCR amplification and purification using AMPure XP beads. RNA and library quality was assessed using an Agilent 2100 Bioanalyzer. Sequencing was carried out using an Illumina NovaSeq 6000 with 150-bp paired-end reads.

Quality control of the RNA sequencing data was performed using FastQC (https://www.bioinformatics.babraham.ac.uk/projects/fastqc/). Raw reads were subjected to adapter trimming and low-quality base removal using Trim Galore (https://www.bioinformatics.babraham.ac.uk/projects/trim_galore). The reads were mapped to the reference genome using HISAT2[21]. Salmon was used to quantify the transcript expression [22]. Differentially expressed genes (DEGs) between the 6-wpi and sham group were determined

using the DESeq2 software ($P < 0.05$, absolute value of fold change >2.0). Spearman's rank correlation analysis was used to evaluate the correlation between transcriptome and proteome profiling.

Targeted proteomic analysis

PRM-targeted proteomics was used to validate the DEPs identified in label-free analysis. The peptides generated from the enzymatic digestion of the proteins were desalted using Pierce™ C18 Tips (87782, Thermo Fisher Scientific) according to the manufacturer's instructions. Quality control samples were prepared by mixing 2 μL of supernatant from each sample (sham group, n=5; 6-wpi group, n=5). DDA of the pooled sample was used to provide the key information required to select peptides (1–3 unique peptides of each protein), including amino acid sequence, retention time, charge state, and m/z value[23]. Selected peptides were monitored using an Orbitrap Fusion™ Tribrid™ High-Resolution Mass Spectrometer coupled to an Easy-nLC ™ liquid chromatography system (Thermo Fisher Scientific) with a 15 cm×75μm column (2μm) at a flow rate of 300 nL/min with a 120 min gradient: (1) 5–10% solvent B for the first 28 min; (2) 10–22% in 55 min; (3) 22–30% in 27 min; (4) and 100% solvent in the last 10 min. A full mass spectrum with a resolution of 60,000, target AGC values of 1.0×10^6, maximum injection time of 50 ms, and m/z values ranging from 350–2000 was followed by an MS/MS scan with a resolution of 30,000, target AGC values of 1.0×10^5, maximum injection time of 100 ms, HCD collision energy of 30%, m/z value range of 120–2000, and isolation window of 1 m/z. The peak area of the ions was used for quantification of the peptides using the Skyline software[24].

Methylated RNA immunoprecipitation and sequencing

Total RNAs was extracted from spinal cord samples (sham group, n=3; 6-wpi group, n=3), followed by the assessment of integrity and concentration using an Agilent 2100 bioanalyzer (Agilent) and a SimpliNano spectrophotometer (GE Healthcare), respectively. Fragmented RNAs (100 nt) were incubated with anti-m^{6}A polyclonal antibody (Merck Millipore) at 4°C for 2 h. Both the immunoprecipitated RNAs and input samples were used for library generation with Ovation SoLo RNA-Seq System Core Kit (NuGEN). The library preparations were subjected to 150 bp paired-end sequencing on the Illumina Novaseq platform according to standard protocols.

The raw data were preprocessed using fastp (version 0.19.11) to obtain clean data[25]. The reads were aligned to the reference genome using the Burrows-Wheeler Alignment tool (BWA, version 0.7.12)[26]. The exomePeak R package (version 2.16.0) was used for m^{6}A peak identification (q-value<0.05) and differential analysis (P <0.05, absolute value of fold-change >1). Motif analysis of m^{6}A peaks was performed using HOMER (version 4.9.1)[27]. Integrative genomics viewer (IGV) software was used to visualize the m^{6}A peaks [28].

Functional enrichment analysis

GO and KEGG pathway enrichment analyses of DEGs, DEPs, and genes with differential m^{6}A modification were performed using the "clusterProfiler" package (version 4.2.2) [29]. Pathway terms with P<0.05 were considered to be statistically significant.

Immunofluorescence staining

Spinal cord tissues were fixed in 4% paraformaldehyde overnight and dehydrated in 12%, 18%, and 24% sucrose solutions at 4°C. A 10 mm spinal cord centered at the injury site was embedded in optimal cutting temperature compound (TissueTek, 4583, Sakura) and cut into 20 μm sections using a Leica CM1950 cryostat. Slices were rinsed thrice in PBS, followed by 30 min blocking using 10% normal donkey serum in 0.01 M PBS and 0.1% Triton X-100 buffer, and incubation with anti-F4/80 (1:200, Cell Signaling Technology 71299S) and anti-LC3A/B (1:200, Cell Signaling Technology 12741S) overnight at RT. After primary antibody incubation, slices were washed thrice in PBS and incubated with donkey anti-rabbit Alexa Fluor 555 (1:200, Abcam ab150062) and donkey anti-rat Alexa Fluor 647 (1:200, Abcam ab150155) at RT for 2 h. For LDs staining, slices were incubated with BODIPY (1:400, Invitrogen D3922) at RT for 20 min. The slices were washed thrice in PBS and mounted with Fluoromount-G (0100-20, Southern Biotech). Images were captured and analyzed using a Zeiss confocal microscope (LSM980, Zeiss, Germany) and ZEISS ZEN 3.3 software.

Oil Red O staining

Slices were pre-warmed and rinsed three times in PBS, followed by 15 min staining with Oil Red O solution and washing with 60% isopropanol for 10 s thrice. The slices were re-stained with hematoxylin, mounted with glycerol, and viewed using a Leica DM4000 microscope.

Statistical analyses

GraphPad Prism (version 8.2.1) was used to conduct statistical analyses. Mann-Whitney test was used to analyze the immunofluorescence and PRM results between the 6-wpi and sham group. P< 0.05 was considered statistically significant.

References

[1] GBD 2016 Traumatic Brain Injury and Spinal Cord Injury Collaborators. Global, regional, and national burden of traumatic brain injury and spinal cord injury, 1990-2016: a systematic analysis for the Global Burden of Disease Study 2016 [J]. Lancet Neurol, 2019, 18(1): 56-87.

[2] Zipser C M, Cragg J J, Guest J D, Fehlings M G, Jutzeler C R, Anderson A J, Curt A. Cell-based and stem-cell-based treatments for spinal cord injury: evidence from clinical trials [J]. Lancet Neurol, 2022, 21(7): 659-70.

[3] Bourguignon L, Tong B, Geisler F, Schubert M, Röhrich F, Saur M, Weidner N, Rupp R, Kalke Y B, Abel

R, Maier D, Grassner L, Chhabra H S, Liebscher T, Cragg J J, Kramer J, Curt A, Jutzeler C R. International surveillance study in acute spinal cord injury confirms viability of multinational clinical trials [J]. BMC Med, 2022, 20(1): 225.

[4] Tran A P, Warren P M, Silver J. The Biology of Regeneration Failure and Success After Spinal Cord Injury [J]. Physiol Rev, 2018, 98(2): 881-917.

[5] Pukos N, Goodus M T, Sahinkaya F R, McTigue D M. Myelin status and oligodendrocyte lineage cells over time after spinal cord injury: What do we know and what still needs to be unwrapped? [J]. Glia, 2019, 67(11): 2178-202.

[6] Zrzavy T, Schwaiger C, Wimmer I, Berger T, Bauer J, Butovsky O, Schwab J M, Lassmann H, Höftberger R. Acute and non-resolving inflammation associate with oxidative injury after human spinal cord injury [J]. Brain, 2021, 144(1): 144-61.

[7] Dorrier C E, Jones H E, Pintarić L, Siegenthaler J A, Daneman R. Emerging roles for CNS fibroblasts in health, injury and disease [J]. Nat Rev Neurosci, 2022, 23(1): 23-34.

[8] Franklin R J M, Ffrench-Constant C. Regenerating CNS myelin - from mechanisms to experimental medicines [J]. Nat Rev Neurosci, 2017, 18(12): 753-69.

[9] Yoon J H, Seo Y, Jo Y S, Lee S, Cho E, Cazenave-Gassiot A, Shin Y S, Moon M H, An H J, Wenk M R, Suh P G. Brain lipidomics: From functional landscape to clinical significance [J]. Sci Adv, 2022, 8(37): eadc9317.

[10] Shafik A M, Zhang F, Guo Z, Dai Q, Pajdzik K, Li Y, Kang Y, Yao B, Wu H, He C, Allen E G, Duan R, Jin P. N6-methyladenosine dynamics in neurodevelopment and aging, and its potential role in Alzheimer's disease [J]. Genome Biol, 2021, 22(1): 17.

[11] Saher G, Brugger B, Lappe-Siefke C, Mobius W, Tozawa R, Wehr M C, Wieland F, Ishibashi S, Nave K A. High cholesterol level is essential for myelin membrane growth [J]. Nat Neurosci, 2005, 8(4): 468-75.

[12] Yao X Q, Liu Z Y, Chen J Y, Huang Z C, Liu J H, Sun B H, Zhu Q A, Ding R T, Chen J T. Proteomics and bioinformatics reveal insights into neuroinflammation in the acute to subacute phases in rat models of spinal cord contusion injury [J]. Faseb j, 2021, 35(7): e21735.

[13] Yao X Q, Chen J Y, Yu Z H, Huang Z C, Hamel R, Zeng Y Q, Huang Z P, Tu K W, Liu J H, Lu Y M, Zhou Z T, Pluchino S, Zhu Q A, Chen J T. Bioinformatics analysis identified apolipoprotein E as a hub gene regulating neuroinflammation in macrophages and microglia following spinal cord injury [J]. Front Immunol, 2022, 13: 964138.

[14] Huang Z, Huang Z, Kong G, Lin J, Liu J, Yang Z, Li R, Wu X, Alaeiilkhchi N, Jiang H, Liu J, Wu X, Zhu Q. Anatomical and behavioral outcomes following a graded hemi-contusive cervical spinal cord injury model

in mice [J]. Behav Brain Res, 2022, 419: 113698.
[15] Sinitcyn P, Tiwary S, Rudolph J, Gutenbrunner P, Wichmann C, Yılmaz Ş, Hamzeiy H, Salinas F, Cox J. MaxQuant goes Linux [J]. Nat Methods, 2018, 15(6): 401.
[16] Zhang X, Smits A H, van Tilburg G B, Ovaa H, Huber W, Vermeulen M. Proteome-wide identification of ubiquitin interactions using UbIA-MS [J]. Nat Protoc, 2018, 13(3): 530-50.
[17] Langfelder P, Horvath S. WGCNA: an R package for weighted correlation network analysis [J]. BMC Bioinformatics, 2008, 9: 559.
[18] Kumar L, M E F. Mfuzz: a software package for soft clustering of microarray data [J]. Bioinformation, 2007, 2(1): 5-7.
[19] Sarafian M H, Gaudin M, Lewis M R, Martin F P, Holmes E, Nicholson J K, Dumas M E. Objective set of criteria for optimization of sample preparation procedures for ultra-high throughput untargeted blood plasma lipid profiling by ultra performance liquid chromatography-mass spectrometry [J]. Anal Chem, 2014, 86(12): 5766-74.
[20] Pang Z, Zhou G, Ewald J, Chang L, Hacariz O, Basu N, Xia J. Using MetaboAnalyst 5.0 for LC-HRMS spectra processing, multi-omics integration and covariate adjustment of global metabolomics data [J]. Nat Protoc, 2022, 17(8): 1735-61.
[21] Kim D, Paggi J M, Park C, Bennett C, Salzberg S L. Graph-based genome alignment and genotyping with HISAT2 and HISAT-genotype [J]. Nat Biotechnol, 2019, 37(8): 907-15.
[22] Patro R, Duggal G, Love M I, Irizarry R A, Kingsford C. Salmon provides fast and bias-aware quantification of transcript expression [J]. Nat Methods, 2017, 14(4): 417-9.
[23] Rauniyar N. Parallel Reaction Monitoring: A Targeted Experiment Performed Using High Resolution and High Mass Accuracy Mass Spectrometry [J]. Int J Mol Sci, 2015, 16(12): 28566-81.
[24] MacLean B, Tomazela D M, Shulman N, Chambers M, Finney G L, Frewen B, Kern R, Tabb D L, Liebler D C, MacCoss M J. Skyline: an open source document editor for creating and analyzing targeted proteomics experiments [J]. Bioinformatics, 2010, 26(7): 966-8.
[25] Chen S, Zhou Y, Chen Y, Gu J. fastp: an ultra-fast all-in-one FASTQ preprocessor [J]. Bioinformatics, 2018, 34(17): i884-i90.
[26] Li H, Durbin R. Fast and accurate short read alignment with Burrows-Wheeler transform [J]. Bioinformatics, 2009, 25(14): 1754-60.
[27] Heinz S, Benner C, Spann N, Bertolino E, Lin Y C, Laslo P, Cheng J X, Murre C, Singh H, Glass C K. Simple combinations of lineage-determining transcription factors prime cis-regulatory elements required for macrophage and B cell identities [J]. Mol Cell, 2010, 38(4): 576-89.

[28] Thorvaldsdóttir H, Robinson J T, Mesirov J P. Integrative Genomics Viewer (IGV): high-performance genomics data visualization and exploration [J]. Brief Bioinform, 2013, 14(2): 178-92.
[29] Wu T, Hu E, Xu S, Chen M, Guo P, Dai Z, Feng T, Zhou L, Tang W, Zhan L, Fu X, Liu S, Bo X, Yu G. clusterProfiler 4.0: A universal enrichment tool for interpreting omics data [J]. Innovation (N Y), 2021, 2(3): 100141.
[30] Dias D O, Kalkitsas J, Kelahmetoglu Y, Estrada C P, Tatarishvili J, Holl D, Jansson L, Banitalebi S, Amiry-Moghaddam M, Ernst A, Huttner H B, Kokaia Z, Lindvall O, Brundin L, Frisén J, Göritz C. Pericyte-derived fibrotic scarring is conserved across diverse central nervous system lesions [J]. Nat Commun, 2021, 12(1): 5501.
[31] Liu N K, Deng L X, Zhang Y P, Lu Q B, Wang X F, Hu J G, Oakes E, Bonventre J V, Shields C B, Xu X M. Cytosolic phospholipase A2 protein as a novel therapeutic target for spinal cord injury [J]. Ann Neurol, 2014, 75(5): 644-58.
[32] Yang D, Wang X, Zhang L, Fang Y, Zheng Q, Liu X, Yu W, Chen S, Ying J, Hua F. Lipid metabolism and storage in neuroglia: role in brain development and neurodegenerative diseases [J]. Cell Biosci, 2022, 12(1): 106.
[33] Singh R, Kaushik S, Wang Y, Xiang Y, Novak I, Komatsu M, Tanaka K, Cuervo A M, Czaja M J. Autophagy regulates lipid metabolism [J]. Nature, 2009, 458(7242): 1131-5.
[34] Robichaud S, Fairman G, Vijithakumar V, Mak E, Cook D P, Pelletier A R, Huard S, Vanderhyden B C, Figeys D, Lavallée-Adam M, Baetz K, Ouimet M. Identification of novel lipid droplet factors that regulate lipophagy and cholesterol efflux in macrophage foam cells [J]. Autophagy, 2021, 17(11):3671-3689
[35] Schulze R J, Krueger E W, Weller S G, Johnson K M, Casey C A, Schott M B, McNiven M A. Direct lysosome-based autophagy of lipid droplets in hepatocytes [J]. Proc Natl Acad Sci U S A, 2020, 117(51): 32443-52.
[36] Itoh N, Itoh Y, Tassoni A, Ren E, Kaito M, Ohno A, Ao Y, Farkhondeh V, Johnsonbaugh H, Burda J, Sofroniew M V, Voskuhl R R. Cell-specific and region-specific transcriptomics in the multiple sclerosis model: Focus on astrocytes [J]. Proc Natl Acad Sci U S A, 2018, 115(2): E302-e9.
[37] Pascua-Maestro R, Diez-Hermano S, Lillo C, Ganfornina M D, Sanchez D. Protecting cells by protecting their vulnerable lysosomes: Identification of a new mechanism for preserving lysosomal functional integrity upon oxidative stress [J]. PLoS Genet, 2017, 13(2): e1006603.
[38] Masuda T, Amann L, Sankowski R, Staszewski O, Lenz M, P D E, Snaidero N, Costa Jordão M J, Böttcher C, Kierdorf K, Jung S, Priller J, Misgeld T, Vlachos A, Meyer-Luehmann M, Knobeloch K P, Prinz M. Novel Hexb-based tools for studying microglia in the CNS [J]. Nat Immunol, 2020, 21(7): 802-15.

[39] Cheng X T, Xie Y X, Zhou B, Huang N, Farfel-Becker T, Sheng Z H. Characterization of LAMP1-labeled nondegradative lysosomal and endocytic compartments in neurons [J]. J Cell Biol, 2018, 217(9): 3127-39.
[40] Hara M, Kobayakawa K, Ohkawa Y, Kumamaru H, Yokota K, Saito T, Kijima K, Yoshizaki S, Harimaya K, Nakashima Y, Okada S. Interaction of reactive astrocytes with type I collagen induces astrocytic scar formation through the integrin-N-cadherin pathway after spinal cord injury [J]. Nat Med, 2017, 23(7): 818-28.
[41] Zhou B, Liu C, Xu L, Yuan Y, Zhao J, Zhao W, Chen Y, Qiu J, Meng M, Zheng Y, Wang D, Gao X, Li X, Zhao Q, Wei X, Wu D, Zhang H, Hu C, Zhuo X, Zheng M, Wang H, Lu Y, Ma X. N(6) -Methyladenosine Reader Protein YT521-B Homology Domain-Containing 2 Suppresses Liver Steatosis by Regulation of mRNA Stability of Lipogenic Genes [J]. Hepatology, 2021, 73(1): 91-103.
[42] Cristobal C D, Wang C Y, Zuo Z, Smith J A, Lindeke-Myers A, Bellen H J, Lee H K. Daam2 Regulates Myelin Structure and the Oligodendrocyte Actin Cytoskeleton through Rac1 and Gelsolin [J]. J Neurosci, 2022, 42(9): 1679-91.
[43] Li Z, Peng Y, Li J, Chen Z, Chen F, Tu J, Lin S, Wang H. N(6)-methyladenosine regulates glycolysis of cancer cells through PDK4 [J]. Nat Commun, 2020, 11(1): 2578.
[44] Matcovitch-Natan O, Winter D R, Giladi A, Vargas Aguilar S, Spinrad A, Sarrazin S, Ben-Yehuda H, David E, Zelada González F, Perrin P, Keren-Shaul H, Gury M, Lara-Astaiso D, Thaiss C A, Cohen M, Bahar Halpern K, Baruch K, Deczkowska A, Lorenzo-Vivas E, Itzkovitz S, Elinav E, Sieweke M H, Schwartz M, Amit I. Microglia development follows a stepwise program to regulate brain homeostasis [J]. Science, 2016, 353(6301): aad8670.
[45] Keerthivasan S, Şenbabaoğlu Y, Martinez-Martin N, Husain B, Verschueren E, Wong A, Yang Y A, Sun Y, Pham V, Hinkle T, Oei Y, Madireddi S, Corpuz R, Tam L, Carlisle S, Roose-Girma M, Modrusan Z, Ye Z, Koerber J T, Turley S J. Homeostatic functions of monocytes and interstitial lung macrophages are regulated via collagen domain-binding receptor LAIR1 [J]. Immunity, 2021, 54(7): 1511-26.e8.
[46] Ryan C B, Choi J S, Al-Ali H, Lee J K. Myelin and non-myelin debris contribute to foamy macrophage formation after spinal cord injury [J]. Neurobiol Dis, 2022, 163: 105608.
[47] Dimas P, Montani L, Pereira J A, Moreno D, Trötzmüller M, Gerber J, Semenkovich C F, Köfeler H C, Suter U. CNS myelination and remyelination depend on fatty acid synthesis by oligodendrocytes [J]. Elife, 2019, 8:e44702
[48] Gouna G, Klose C, Bosch-Queralt M, Liu L, Gokce O, Schifferer M, Cantuti-Castelvetri L, Simons M. TREM2-dependent lipid droplet biogenesis in phagocytes is required for remyelination [J]. J Exp Med, 2021, 218(10):e20210227

[49] Scorletti E, Carr R M. A new perspective on NAFLD: Focusing on lipid droplets [J]. J Hepatol, 2022, 76(4): 934-45.
[50] Luo J, Yang H, Song B L. Mechanisms and regulation of cholesterol homeostasis [J]. Nat Rev Mol Cell Biol, 2020, 21(4): 225-45.
[51] Vitali C, Wellington C L, Calabresi L. HDL and cholesterol handling in the brain [J]. Cardiovasc Res, 2014, 103(3): 405-13.
[52] Zelcer N, Hong C, Boyadjian R, Tontonoz P. LXR regulates cholesterol uptake through Idol-dependent ubiquitination of the LDL receptor [J]. Science, 2009, 325(5936): 100-4.
[53] Berghoff S A, Spieth L, Sun T, Hosang L, Schlaphoff L, Depp C, Düking T, Winchenbach J, Neuber J, Ewers D, Scholz P, van der Meer F, Cantuti-Castelvetri L, Sasmita A O, Meschkat M, Ruhwedel T, Möbius W, Sankowski R, Prinz M, Huitinga I, Sereda M W, Odoardi F, Ischebeck T, Simons M, Stadelmann-Nessler C, Edgar J M, Nave K A, Saher G. Microglia facilitate repair of demyelinated lesions via post-squalene sterol synthesis [J]. Nat Neurosci, 2021, 24(1): 47-60.
[54] Blanchard J W, Akay L A, Davila-Velderrain J, von Maydell D, Mathys H, Davidson S M, Effenberger A, Chen C Y, Maner-Smith K, Hajjar I, Ortlund E A, Bula M, Agbas E, Ng A, Jiang X, Kahn M, Blanco-Duque C, Lavoie N, Liu L, Reyes R, Lin Y T, Ko T, R'Bibo L, Ralvenius W T, Bennett D A, Cam H P, Kellis M, Tsai L H. APOE4 impairs myelination via cholesterol dysregulation in oligodendrocytes [J]. Nature, 2022, 611(7937):769-779.

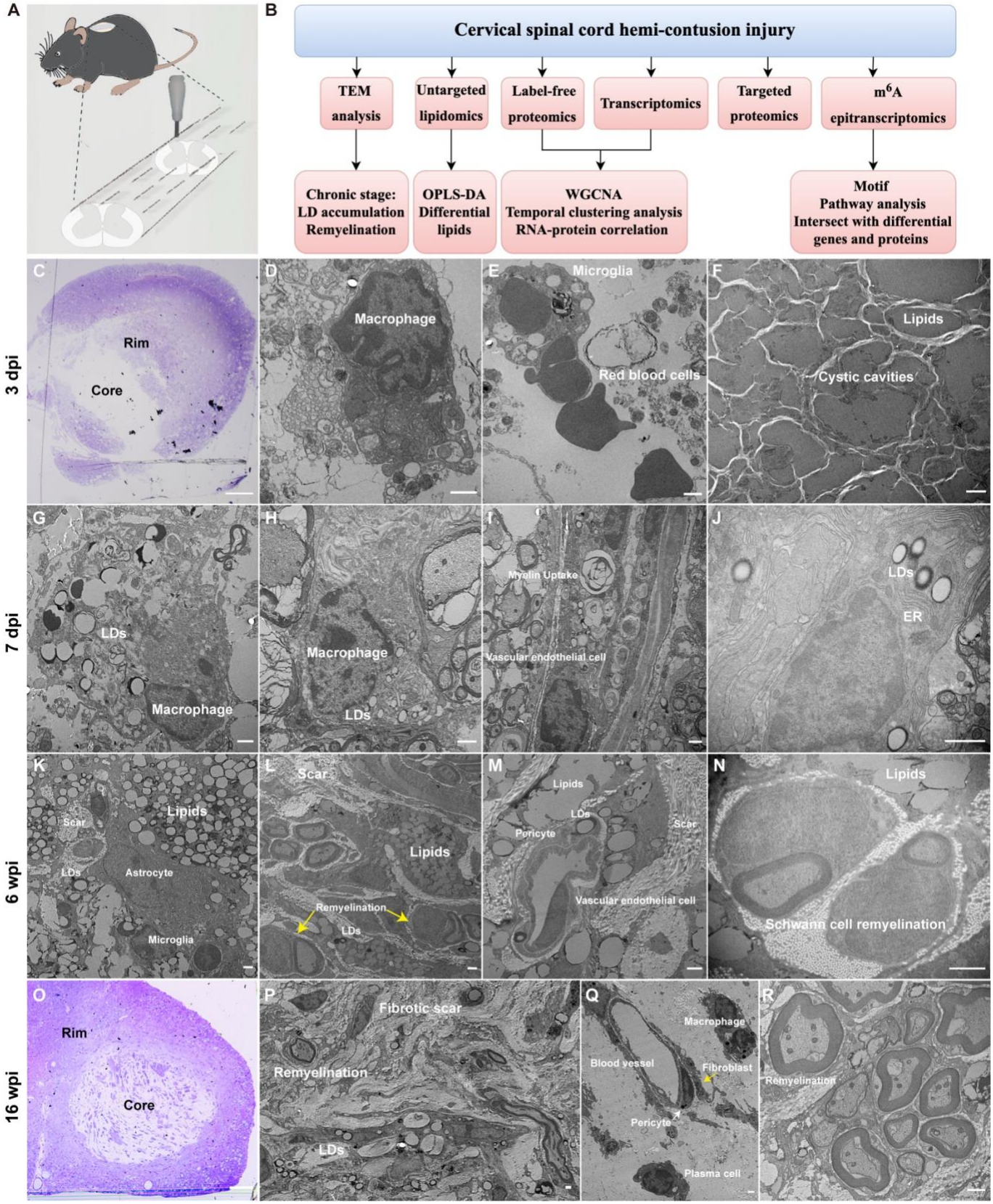

Fig.1 Time-course analysis of transmission electron microscopy (TEM) images in a mouse spinal cord injury (SCI) model. **a** Schematic illustration of the C5 spinal cord hemi-contusion injury. **b** Scheme for the integrated analysis of ultrastructural characteristics and multi-omics. **c** Toluidine blue staining of semi-thin sections sampled three days post injury (dpi). **d-f** TEM images of lesions sampled 3-dpi. **g-j** TEM images of lesions sampled 7-dpi. LDs, lipid droplets. ER, endoplasmic reticulum. **k-n** TEM images of lesions sampled six weeks

post injury (wpi). Yellow arrows, remyelination. **o** Toluidine blue staining of semi-thin sections sampled 16-wpi. **p-r** TEM images of lesions sampled 16-wpi. Yellow arrow, fibroblast. White arrow, pericyte. Scale bar (c, o) = 100 µm. Scale bar (d-n, p-r) = 1 µm.

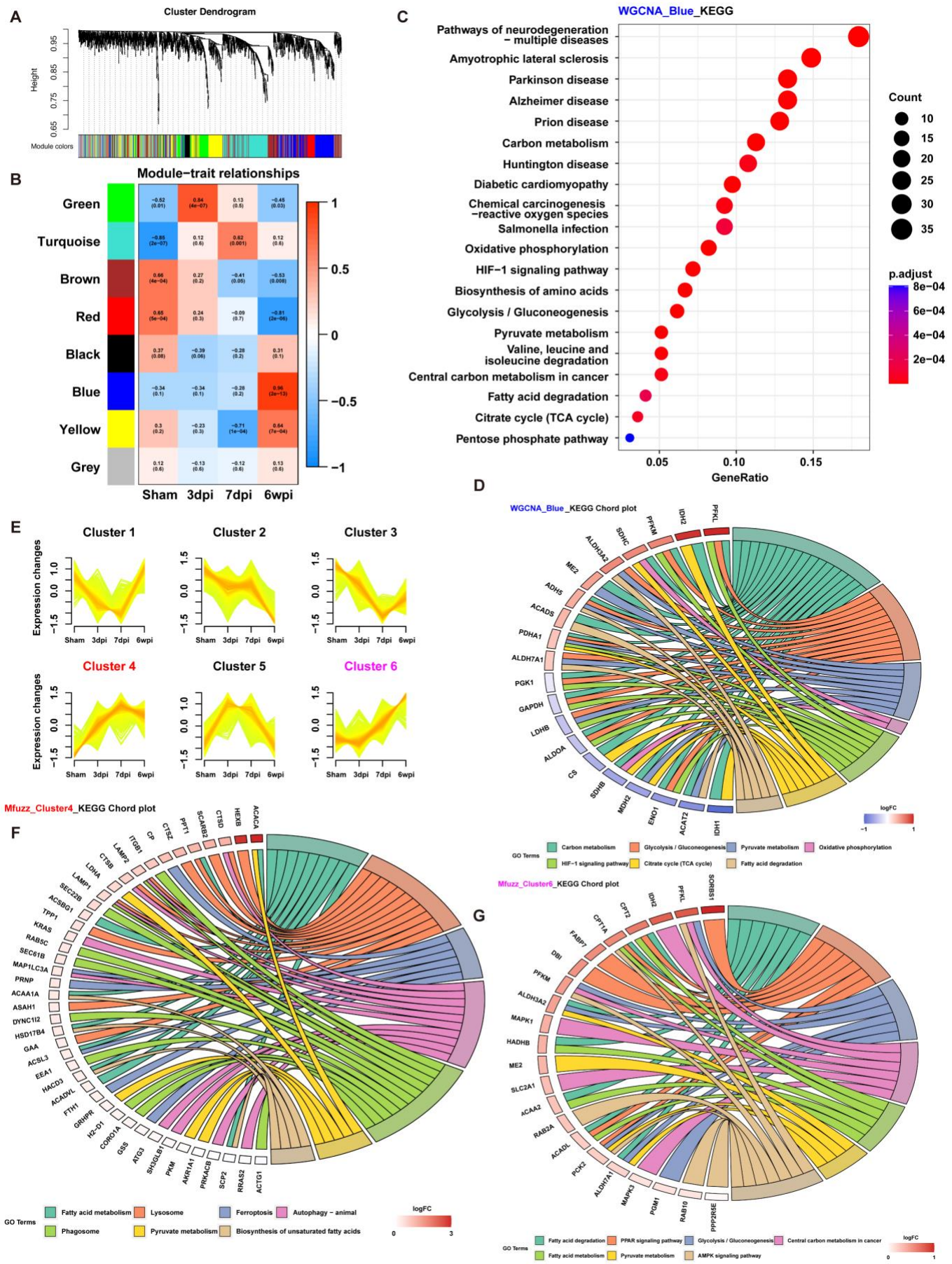

Fig.2 WGCNA and temporal clustering analysis of untargeted proteomic profiling in spinal cord samples at three phases of SCI. **a, b** Clustering dendrogram (a) and module-trait relationships (b) of 24 samples showing

distinct coexpression modules identified by WGCNA. **c, d** Bubble plot (c) and chord plot (d) showing the KEGG pathway enrichment analysis of the proteins in the blue module. **e** Temporal clustering analysis identifying six distinct clusters using fuzzy c-means algorithm. **f, g** Chord plot showing the KEGG pathway enrichment analysis of the proteins in the cluster 4 (f) and cluster 6 (g).

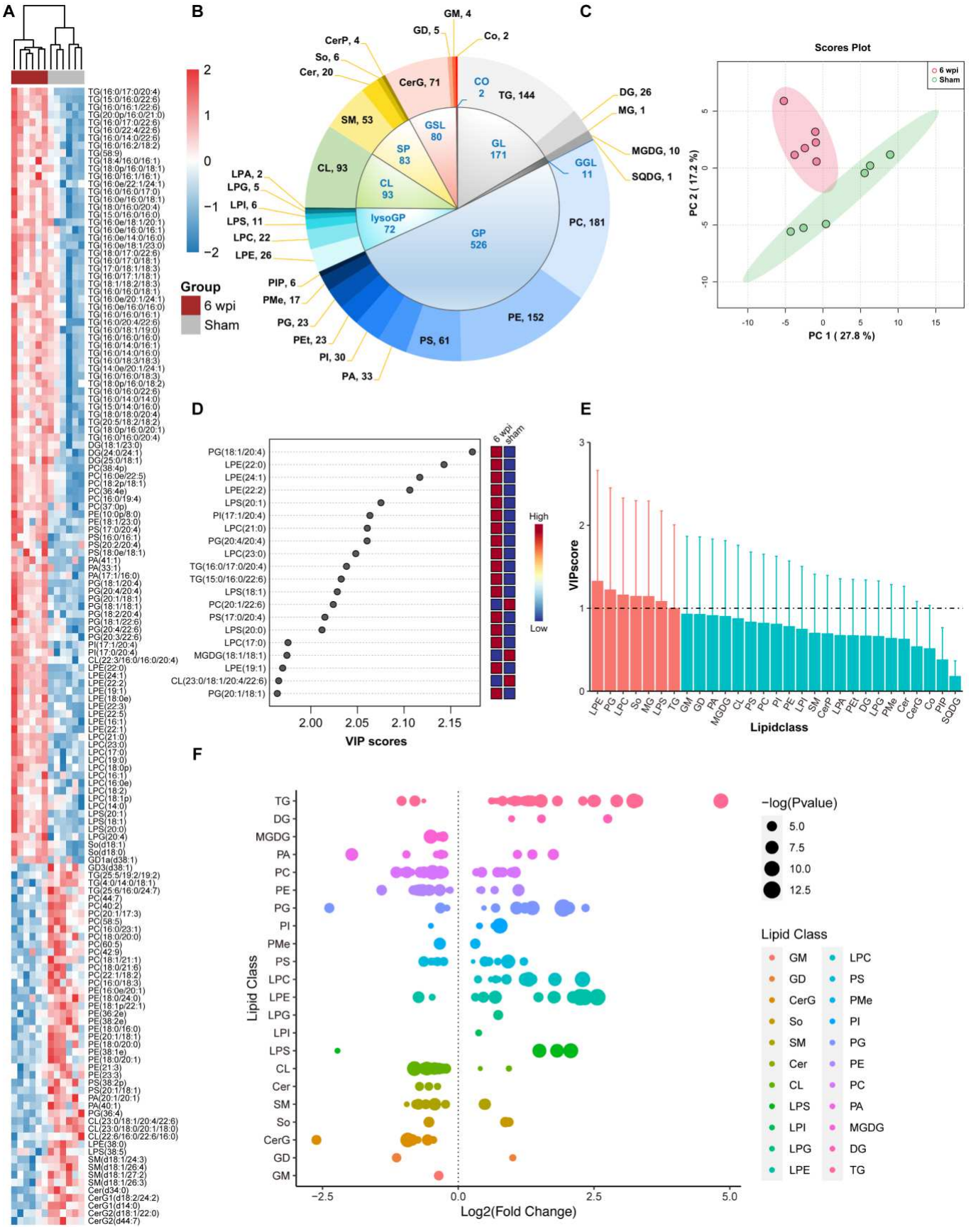

Fig.3 Untargeted lipidomic analysis of the spinal cord samples at the chronic phase of SCI. **a** Heatmap showing the 148 critical lipid species with differential changes ($P < 0.05$, VIP >1, absolute value of fold change >1.5). **b** Pie chart showing the distribution of the 1038 individual lipid species in the lipid classes. **c** Principal component analysis of the lipid profiling from 12 differentiated samples. **d** The top 20 critical lipids

identified by orthogonal projections to latent structures discriminant analysis (OPLS-DA). **e** The variable importance in projection (VIP) scores of lipid classes obtained from OPLS-DA. **f** Bubble plot showing the distribution and corresponding concentration of 235 critical lipid species ($P < 0.05$, VIP >1).

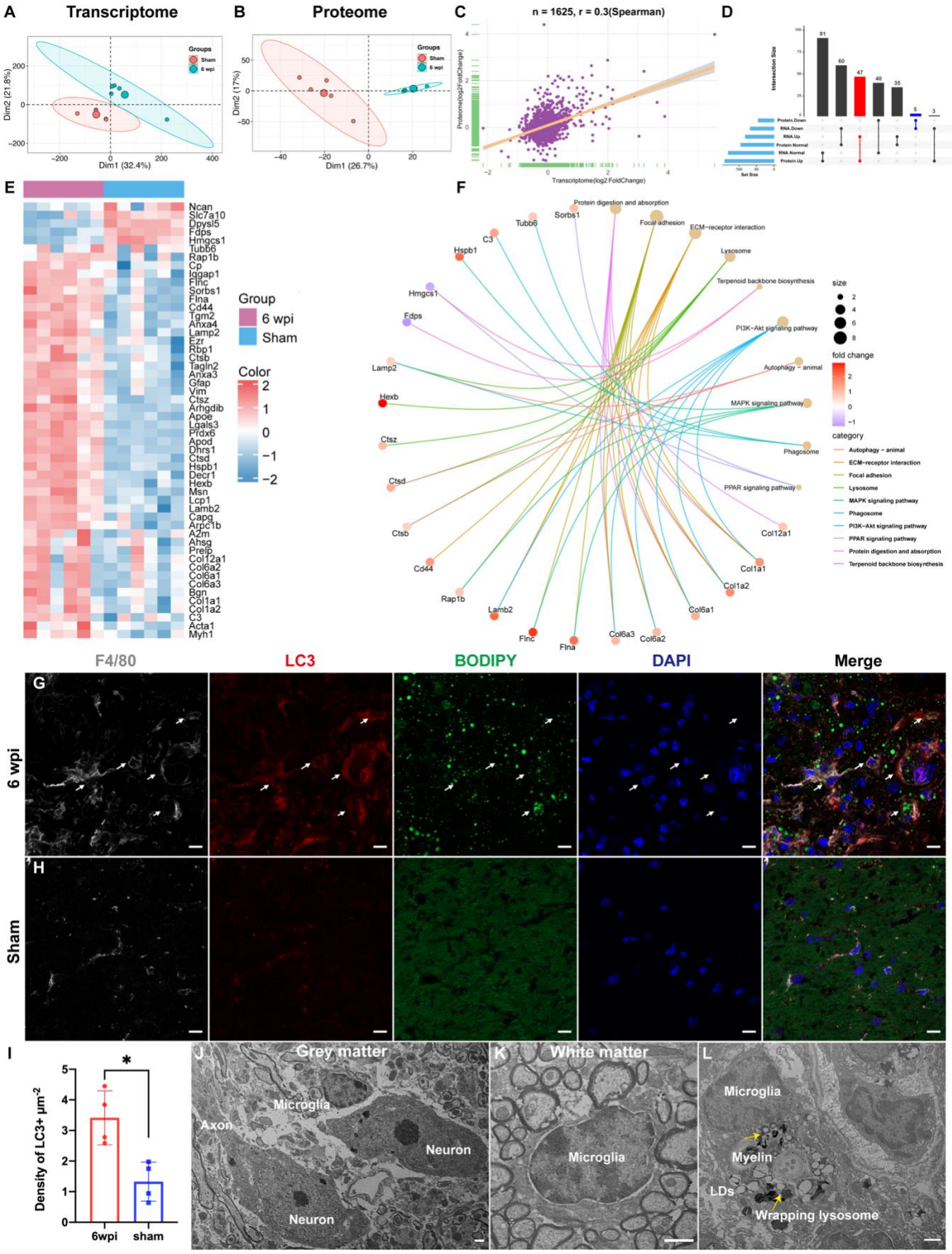

Fig.4 Integrated analysis of the transcriptome and proteome profiling at the chronic phase of SCI. **a, b** Principal component analysis showing good intra consistency and inter-group difference at both RNA (a) and protein (b) levels. **c** The correlation between mRNA levels and protein abundance. **d** Upset plot showing

dysregulated genes at both RNA and protein levels. **e** Heatmap showing the 52 mutual upregulated and downregulated genes in the 12 proteome samples. **f** Chord plot showing the KEGG pathway enrichment analysis of the mutual upregulated and downregulated genes. **g, h** Immunofluorescence staining showing colocalization of LC3 (red) and BODIPY (green) in the F4/80+ microglia/ macrophages (white) at 6-wpi (white arrow). **i** The expression of LC3 was significantly increased at 6-wpi. *P < 0.05. **j, k** Representative TEM images of normal microglia in the gray matter (j) and white matter (k). **l** Representative TEM image of microglia sampled 6-wpi showing abundant inclusions, including myelin, LDs, and different stages of lysosomes. LDs were directly engulfed by the "wrapping lysosomes" (yellow arrows). Scale bar (g, h) =10 μm. Scale bar (j–l) = 1 μm.

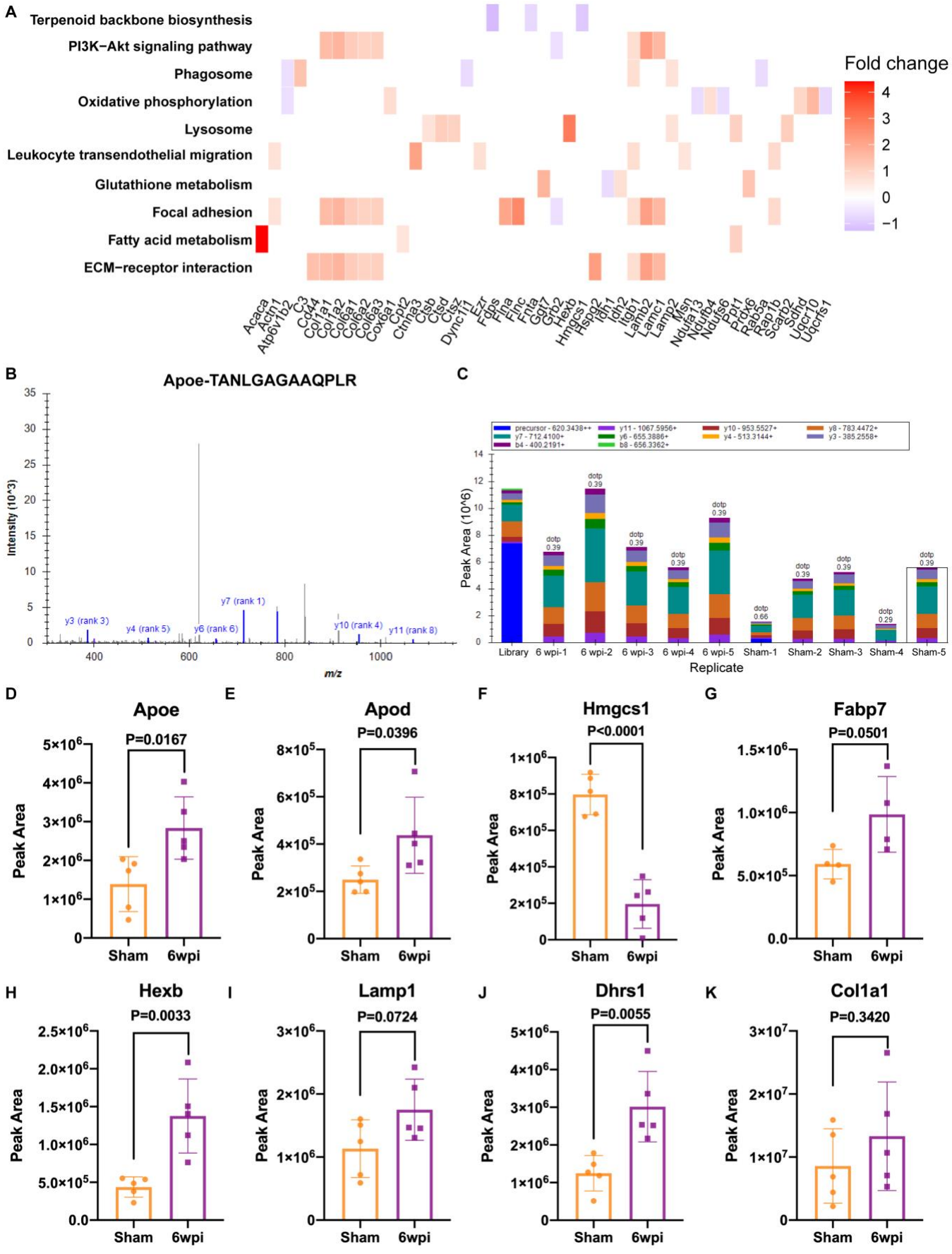

Fig.5 Parallel reaction monitoring (PRM) targeted proteomics. **a** KEGG pathway enrichment analysis of the

Differentially expressed proteins (DEPs) at 6-wpi. **b, c** Representative images of transition identification of peptide and peak area integration using skyline. **d-k** Expression levels of several proteins identified by PRM-targeted proteomics.

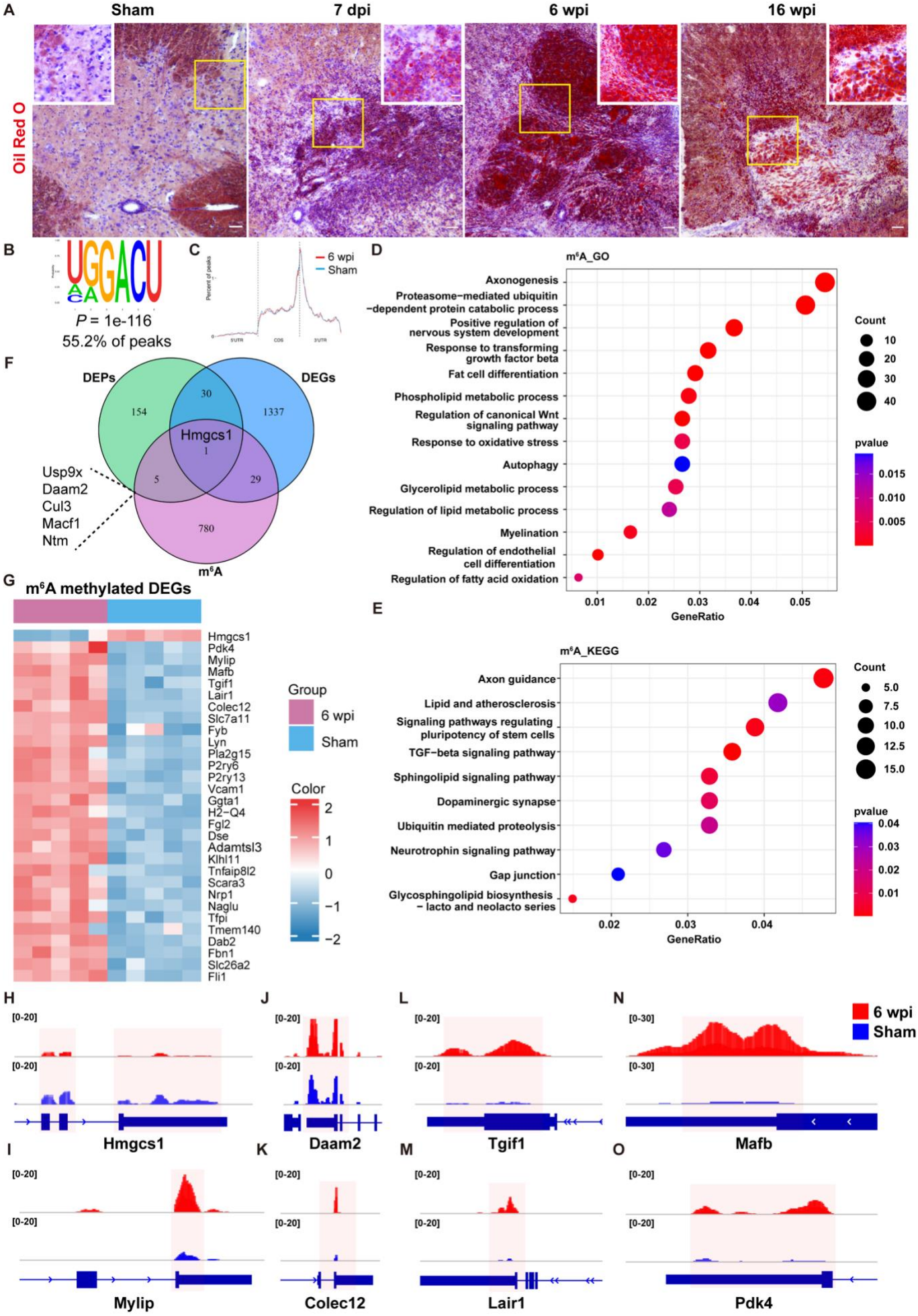
A
Sham
7 dpi
6 wpi
16 wpi
Oil Red O
B
P = 1e-116
55.2% of peaks
C
6 wpi
Sham
D
m⁶A_GO
Axonogenesis
Proteasome−mediated ubiquitin −dependent protein catabolic process
Positive regulation of nervous system development
Response to transforming growth factor beta
Fat cell differentiation
Phospholipid metabolic process
Regulation of canonical Wnt signaling pathway
Response to oxidative stress
Autophagy
Glycerolipid metabolic process
Regulation of lipid metabolic process
Myelination
Regulation of endothelial cell differentiation
Regulation of fatty acid oxidation
GeneRatio
Count
pvalue
E
m⁶A_KEGG
Axon guidance
Lipid and atherosclerosis
Signaling pathways regulating pluripotency of stem cells
TGF−beta signaling pathway
Sphingolipid signaling pathway
Dopaminergic synapse
Ubiquitin mediated proteolysis
Neurotrophin signaling pathway
Gap junction
Glycosphingolipid biosynthesis − lacto and neolacto series
GeneRatio
Count
pvalue
F
DEPs
DEGs
m⁶A
154
30
1337
Hmgcs1
1
5
29
780
Usp9x
Daam2
Cul3
Macf1
Ntm
G
m⁶A methylated DEGs
Hmgcs1
Pdk4
Mylip
Mafb
Tgif1
Lair1
Colec12
Slc7a11
Fyb
Lyn
Pla2g15
P2ry6
P2ry13
Vcam1
Ggta1
H2−Q4
Fgl2
Dse
Adamtsl3
Klhl11
Tnfaip8l2
Scara3
Nrp1
Naglu
Tfpi
Tmem140
Dab2
Fbn1
Slc26a2
Fli1
Group
6 wpi
Sham
Color
H
Hmgcs1
J
Daam2
L
Tgif1
N
Mafb
I
Mylip
K
Colec12
M
Lair1
O
Pdk4
6 wpi
Sham

Fig.6 m^6A profiling of the spinal cord samples at the chronic phase of SCI. **a** Oil red O staining showing lipid accumulation in the lesion of chronic phase. High-magnification images of the yellow boxes are shown in the white boxes. **b** Canonical GGACU motif of m^6A peaks. **c** The distribution of m^6A sites in the transcript regions. CDS, coding sequence; UTR, untranslated region. **d, e** Biological processes by GO analysis (d) and KEGG pathway enrichment analysis (e) of the 815 genes with differential m^6A peaks. **f** Venn diagram showing overlap of the differentially methylated genes, DEPs and DEGs. **g** Heatmap showing the 30 DEGs with differential m^6A peaks. **h-o** IGV screenshots showing differential m^6A peaks in several DEPs and DEGs.

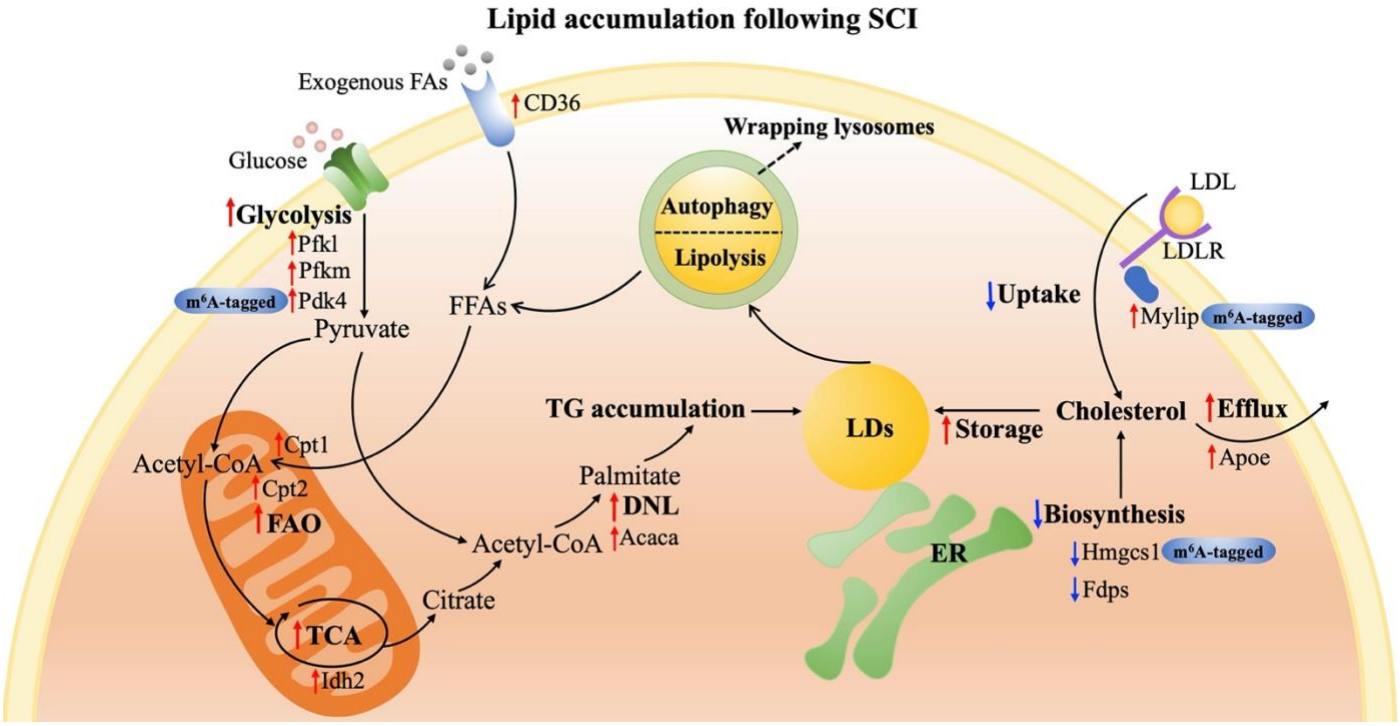

Fig.7 Schematic illustration of molecular changes associated with lipid accumulation following SCI. FAs, fatty acids; FFAs, free fatty acids; FAO, fatty acid oxidation; TCA, tricarboxylic acid; DNL, de novo lipogenesis; TG, triglyceride; LDs, lipid droplets; ER, endoplasmic reticulum; LDL, low-density lipoprotein; LDLR, LDL receptor.